Enhanced fracture resistance of thermoset/thermoplastic interfaces through crack trapping in a morphology gradient

Quentin Voleppe[a], Wael Ballout [a*], Pascal Van Velthem[a], Christian Bailly[a], Thomas Pardoen[b]

[a]Institute of Condensed Matter and Nanosciences - Bio & Soft Matter (IMCN/BSMA), UCLouvain, 1348, Louvain-la-Neuve, Belgium

[b]Institute of Mechanics, Materials and Civil Engineering, UCLouvain, 2 Place Sainte Barbe, 1348 Louvain-la-Neuve, Belgium

KEYWORDS: Composite bonding, Interdiffusion, Interface toughening, Crack trapping, morphology gradient.

ABSTRACT

The hybrid assembling of thermoplastics with thermosets through controlled interdiffusion is an attractive approach towards integrated structural composite bonding. The fracture toughness of the interphase between the high Tg thermoplastic polyetherimide and the RTM6 epoxy is found to be four times higher than the corresponding RTM6 value under specific curing cycle. The origin of this remarkable cracking resistance is elucidated by analyzing the crack path in relationship with the morphology and local elastoplastic and fracture properties of the interphase. The crack is trapped inside a morphological gradient involving a relatively low PEI concentration. Uniaxial compression and nanoindentation tests on homogenous blends exhibit an unexpected softening in this PEI content window. This efficient crack trapping mechanism originates thus from a synergistic coupling between a lower local strength and higher local fracture toughness. This finding opens to many new options for interface toughening beyond the system addressed in this research.

[*] Corresponding author. E-mail address: wael.ballout@uclouvain.be (W. Ballout)
Phone: +32 10 47 82 33

1. INTRODUCTION

The use of fiber reinforced polymer (FRP) composites keeps growing at a very fast pace in both civil and military aircrafts, as motivated by weight reduction constraints and integrated manufacturing opportunities [1], [2], [3], [4]. However, a major limiting factor for further expansion of composite technologies remains the high cost of the raw materials, of the manufacturing and assembly methods [5]. In particular, the joining of composite components constitutes a major cost driver for the development of complex composite structures, due to the different characteristics of FRP composites compared to traditional metallic materials [6]. Consequently, the development of efficient and flexible joining techniques for composite structures has become a critical step for cost-effective manufacturing, as well as for the repair and replacement of modern aircraft components [7], [8], [9], [10].

Three major joining technologies are currently used in aerospace composite structures, namely mechanical fastening, adhesive bonding, and welding (fusion bonding) [8], [9], [10], [11]. Structural adhesive bonding relying mainly on epoxy adhesives has several advantages over mechanical fastening but is labor-intensive due to surface preparation steps and long curing times [12].

Welding, or fusion bonding, is a long-established technology for joining metals or thermoplastics. Composite welding, using thermoplastics as hot-melt adhesives with minimum or little, if any, pre-treatment, is a very efficient process for joining FRP composite components, capable of producing high performance joints, which are equivalent or better than adhesively bonded or mechanically fastened joints [13], [14]. The main advantages of thermoplastic welding over thermoset-based adhesive bonding involve the high rate at which components can be assembled owing to short cycle time and the eco-efficiency of the method, owing to the reduction, or even complete elimination, of for surface preparation [15], [16], [17].

Today, fully cured thermoset composite structural components are essentially joined through mechanical fasteners and/or traditional thermoset adhesives. Due to the highly cross-linked structure, no direct welding can be performed to directly bond thermoset-based composite parts. To take advantage of fusion bonding, several approaches have been undertaken to indirectly join thermoset-based composites by welding, through the use of thermoplastic–thermoset (TS-TP) hybrid adhesives or of a thermoplastic medium layer [15], [18], [19], [20], [21-29]. But a sufficiently tough thermoplastic–thermoset interface is vital to ensure adequate joint performances. Generally, although the level of adherence depends on a number of physical and chemical factors [30-42], proper joint toughness can be achieved when the two polymers are compatible and the molecules can diffuse over a sufficiently large distance to create entanglements on both sides of the interface [43-45]. The resulting interphase morphology suppresses the possibility of easy low-cohesion crack path and favors the generation of extra dissipation mechanisms at the crack tip.

The fracture toughness of TS-TP interphases can be increased by the presence of a co-continuous phase layer inside the morphological gradient as reported for polyetherimide (PEI)-epoxy systems [46-47]. The same trend has also been found by Min et al. [48] on polysulfone-epoxy interphases with dual phase morphology and by Kim et al. [49] on PEI-dicyanate interphases with nodular morphology. The fracture toughness increases linearly with the thickness of the interfacial layers following a well-known trend in structural adhesive bonding in the range of thin bond lines [50-52].

Similar results have been reported for homogeneous TS-TP blends. For instance, Mimura et al. [53] found that the fracture toughness of PES-epoxy systems significantly increases when a co-continuous phase morphology is formed. Only slight improvements are obtained at lower TP-contents corresponding to a sea-island structure. In the latter case, crack branching due to the presence of dispersed PES particles seems to be the main, although limited, toughening mechanism. On the other hand, in the case of a co-continuous morphology, the crack is forced to partly propagate through the tough PES phase, giving rise to a drastic improvement of the fracture toughness. In an earlier study,

Girard-Reydet et al. [54] found similar results in PEI-epoxy blends, the fracture toughness being significantly increased only with the generation of a co-continuous or dispersed morphology. In this case, the main origin of the toughening is the plastic drawing of the PEI-rich phase around undamaged epoxy domains owing to mechanical interlocking, and this, despite a poor interfacial adhesion. In the case of a sea-island structure, the damage resistance is only slightly improved compared to the neat resin. Three different mechanisms appear concurrently active. First, the relatively poor interfacial adhesion in this system prevents significant plastic drawing of the PEI particles and induces debonding, generating microcracks at the interface which then propagate in the material. The particles also act as impenetrable obstacles, forcing the crack to bow, hence generating a crack-pinning mechanism. Finally, particle-induced shear yielding of the TS-rich matrix is also observed.

Surprisingly, the elastoplastic properties of TS-TP blends, either as a research subject in itself or as a necessary ingredient towards a better understanding of the fracture resistance of the corresponding interphases, have not been widely studied so far, and this, despite a potentially significant influence on the amplitude of plastic dissipation upon crack propagation.

Recently, a detailed report on the morphology development upon curing of PEI-RTM6 interfaces addressed the influence of the curing cycle [55]. Here, an original crack trapping phenomenon inside the interfacial composition/morphology gradient is observed in the same system (taken as an important and representative example of a high performance TS-TP interface) leading to remarkable interface cracking resistance in some cases. The fundamental objective of the present work is to unravel the origin of the unusual interfacial failure mechanism at the origin of the good toughness and to relate it to the elastoplastic properties of the mixed TP-TS compositions in the interface zone. As far as we know, such a link has not been established yet. To this end, various RTM6-PEI homogeneous blends and graded interphases have also been generated using different curing cycles. The blends have been characterized by uniaxial compression and nanoindentation while the interphases have been tested by three-point bending tests and the corresponding fracture surfaces analyzed by optical microscopy (OM) and/or

scanning electron microscopy (SEM).

2. MATERIALS AND METHODS

This section describes the constituent materials, the processing of the homogeneous blends and of the different interphases, followed by the mechanical tests and characterization methods.

2.1. Constituent materials

The glassy thermoplastic polymer considered in this study is the polyetherimide (PEI) grade ULTEM 1000 from SABIC Innovative Plastics provided in pellets form, characterized by a molar mass of 50000 g/mol and a Tg of 220 °C. Films of 100 µm thickness were processed using a DSM Xplore Micro Film device. The high crosslinking density thermosetting network consists of the pre-blended epoxy-amine Hexflow RTM6 from Hexcel. The glass transition temperature measured by DSC is equal to -15 °C in the uncured state and reaches 220 °C after curing according to the cycles reported below. In addition, a 30 µm thick polyimide (PI) film from DUPONT is used as crack initiator (see below) intercalated at the RTM6-PEI interphase, see next.

2.2. Processing of homogeneous blends and RTM6-PEI interphases

RTM6-PEI homogenous blends with compositions 0-100, 5-95, 10-90, 15-85, 25-75, 100-0 (RTM6 wt% - PEI wt%) have been prepared for testing and characterization. The processing involves four consecutive steps: (i) the PEI is first dissolved in dichloromethane at room temperature (PEI and RTM6 epoxy precursor are fully miscible in dichloromethane, the latter being a good solvent for both. The solution was optically transparent and remained so upon evaporation of the solvent at 90°C.); (ii) once the PEI is fully dissolved, the RTM6 monomers are mixed providing an optically transparent solution as expected from the good miscibility; (iii) once the RTM6 is fully dissolved, the solution is degassed under vacuum at 90°C for 1 hour; (iv) the sample is then subjected to a temperature cycle for curing consisting of heating ramp of 0.2 °C/min from 90°C up to 180 °C, holding of 2 hours at 180°C, followed

by a cooling ramp at 2 °C/min (this cycle will be further referred as $C_{180,slow}$). Note that above 15% PEI, only very small samples could be produced due to a sharp increase of the viscosity when increasing the PEI content, too small for machining macroscopic mechanical test specimens.

The specimens with RTM6-PEI interphases are processed using an aluminum mold, with dimensions indicated in Figure 1, composed of two identical parts (1) attached together using two threaded rods (2) and two bolts (3). The threaded rods are covered with a thin teflon film in order to avoid any blockage in the case of an uncontrolled flow of the RTM6 reactive monomers due to potential leakage. In order to facilitate the extraction of the cured samples as well as the cleaning after use, all surfaces in contact with the RTM6 during the curing are coated with a demolding agent FREKOTE 700-NC/PINT from HENKEL. A 100 µm thick PEI film (4) as well as a PI insert (5) are placed between two teflon films (6) and the assembly is fixed in between the two parts of the mold by mechanical fastening. The role of the teflon films is again to prevent any leakage. After closing the mold, the epoxy precursor is poured into the lower part (7) followed by degassing under vacuum at 90°C during 1 hour. The additional open space left at the upper part (8) reduces the risk of bubble projections. A temperature cycle is then applied. After curing, the sample is extracted and machined to the right dimensions.

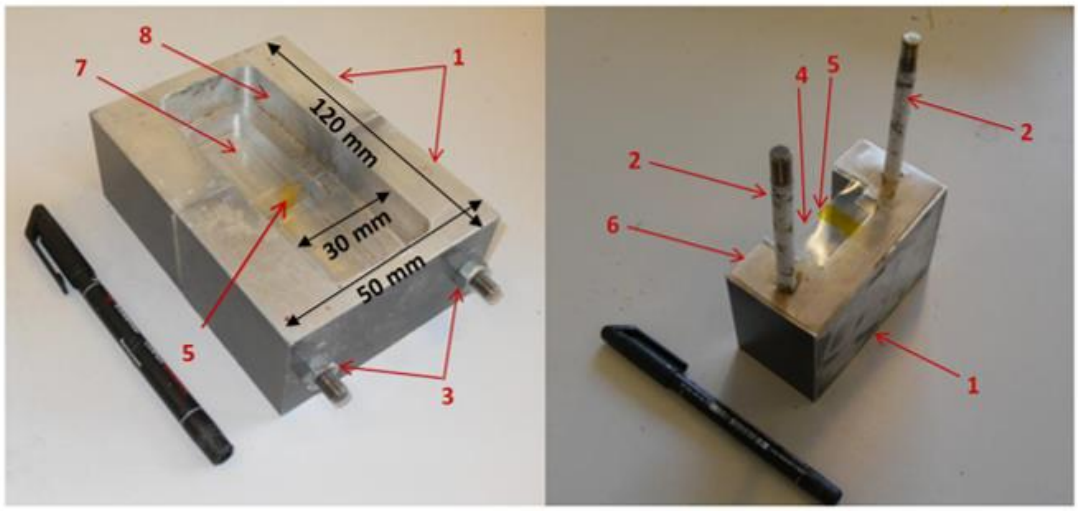

Figure 1. Instrumented mold (1) dedicated to the processing of the specimens containing the TS-TP interphases: (2) two threaded rods; (3) two bolts; (4) PEI film; (5) PI insert; (6) two Teflon films; (7) lower part; (8) upper part.

Three different curing cycles, compared in Figure 2, have been considered. The gel time for each cycle is indicated and determined as the crossover time between the storage and loss moduli obtained from dynamic moduli measurements in a Bohlin Gemini rheometer using plate-plate geometry. Each cycle starts with a degassing step of 60 min under vacuum at 90°C. The $C_{180,slow}$ cycle is the slowest with a heating ramp of 0.2°C/min from 90°C up to 180°C, an holding for 2 hours at 180°C, followed by a cooling ramp at 2°C/min. The C_{180} cycle is identical except for a larger heating rate equal to 0.5°C/min. The C_{160} cycle is the fastest with a heating rate of 2°C/min. For the latter cycle, an intermediate isothermal step of 90 min at 160°C is introduced in order to avoid any overheating or burning of the samples.

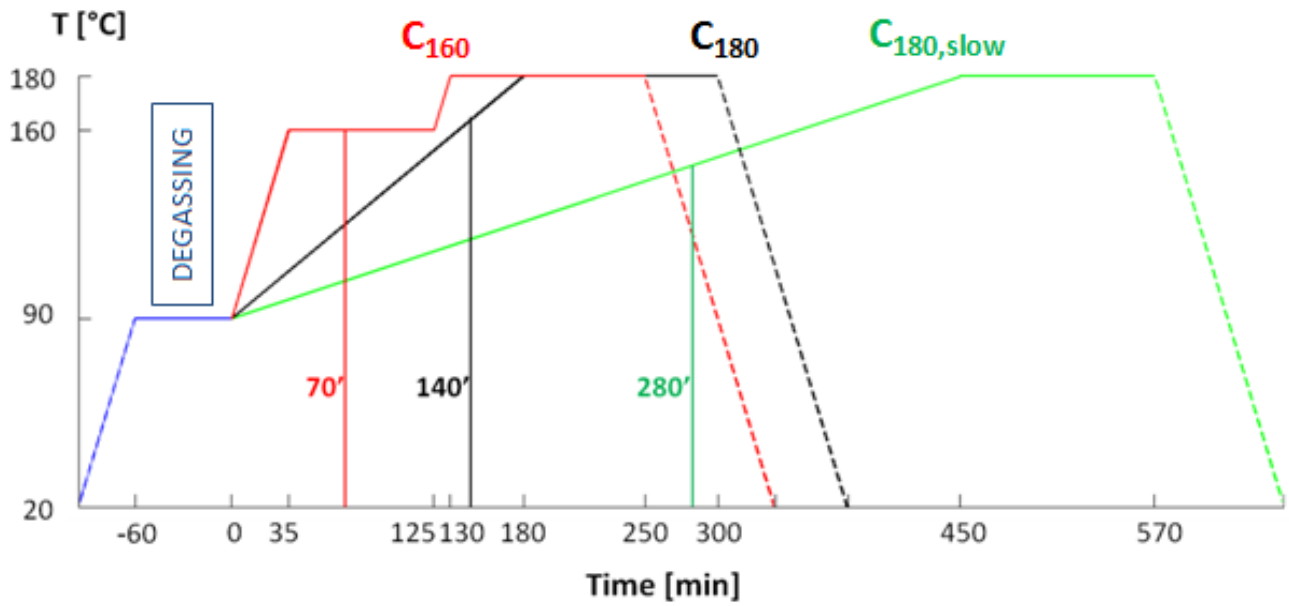

Figure 2. Temperature cycles applied to the TS-TP blends and interphases. The degassing step in blue is common to all cycles while the gel time for each of them is indicated by a vertical segment of the same color.

2.3. Mechanical test procedures

Uniaxial compression tests are performed following the ASTM-D695 standard procedure [56]. The specimens are cylinders with both height and diameter equal to 10 mm. The cylinder is inserted in a Wyoming Test Fixture sub-press to ensure axial alignment. The sub press is mounted on a Zwick Z250

Roell machine equipped with the 250 kN load cell. A constant crosshead displacement rate of 1 mm/min is applied. In addition, solid lubrification using 70 μm thick teflon films is systematically used in order to avoid excessive friction with the compression platens, which can lead to significant barreling [57].

Nanoindentation tests are performed on a G200 nano-indenter by Agilent Technologies using a pyramidal Berkovich diamond indenter. Prior to testing, the surface is prepared by microtomy using a histodiamond knife from Diatome mounted on a Reichert instrument. The elastic modulus and hardness are extracted using the Oliver and Pharr method [58] and averaged over 16 different indents for each specimen. For each indent, the indentation depth is taken in the range between 1 and 2 μm in order to avoid artefacts at small indentation depths related in particular to possible size effects.

The mode I fracture toughness at cracking initiation of an interphase as expressed by K_{Ic} or G_{Ic} is determined by three-point bending of single edge notched bend (SENB) specimens following the standard ASTM-D5045 [59]. The geometry of the specimens and test configuration are shown in Figure 3. The width W is set equal to 14 mm in order to ensure small scale yielding conditions. The bending support is mounted on a Zwick Z250 Roell machine equipped with a 250 kN load cell applying the compressive load at a constant crosshead displacement rate of 1 mm/min while the load-displacement curve is recorded. A valid fracture mechanics test requires the starter crack to be very sharp. Pre-cracking by sliding or tapping a fresh razor blade across the 0.3 mm notch root was not possible due to inaccurate positioning with respect to the RTM6-PEI interphase. This is why a PI insert was introduced next to the PEI film, as explained earlier, serving as a sharp crack initiator owing to its weak adhesion.

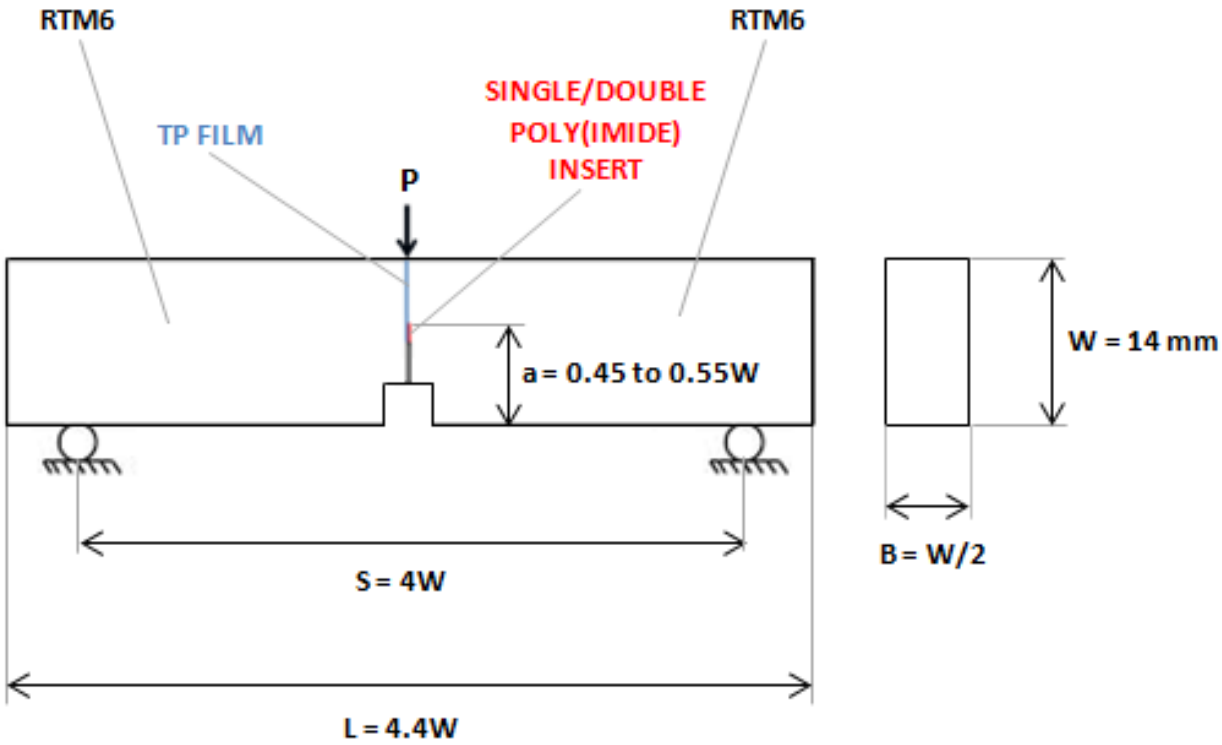

Figure 3. SENB specimens with a precrack located for fracture along TS-TP interphase, following the standard ASTM-D5045.

2.4. Fracture surface and microstructure characterization methods

The fracture surfaces of the broken SENB specimens are characterized along the two views illustrated in Figure 4. The crack path is observed either from face A for a direct/front view of the propagation plane or from face B for a lateral view in order to position the crack path along the interphase. The metallized surfaces of the front views (face A) are characterized by scanning electron microscopy (SEM) using a Jeol FEG SEM 7600F. The metallization consists in the deposition of a 10 nm gold layer on the surfaces in order to avoid electrostatic charging. The lateral views (face B) are observed by phase contrast optical microscopy (OM) on a TH4/200 Olympus microscope using 200 nm thick microtomed slices extracted from the extremities of the lateral sides of the fracture surfaces. Similar to the lateral views of the fracture surfaces, the morphology of homogenous blends as well as the morphological gradients at the interphases are also characterized by phase contrast OM using microtomed layers.

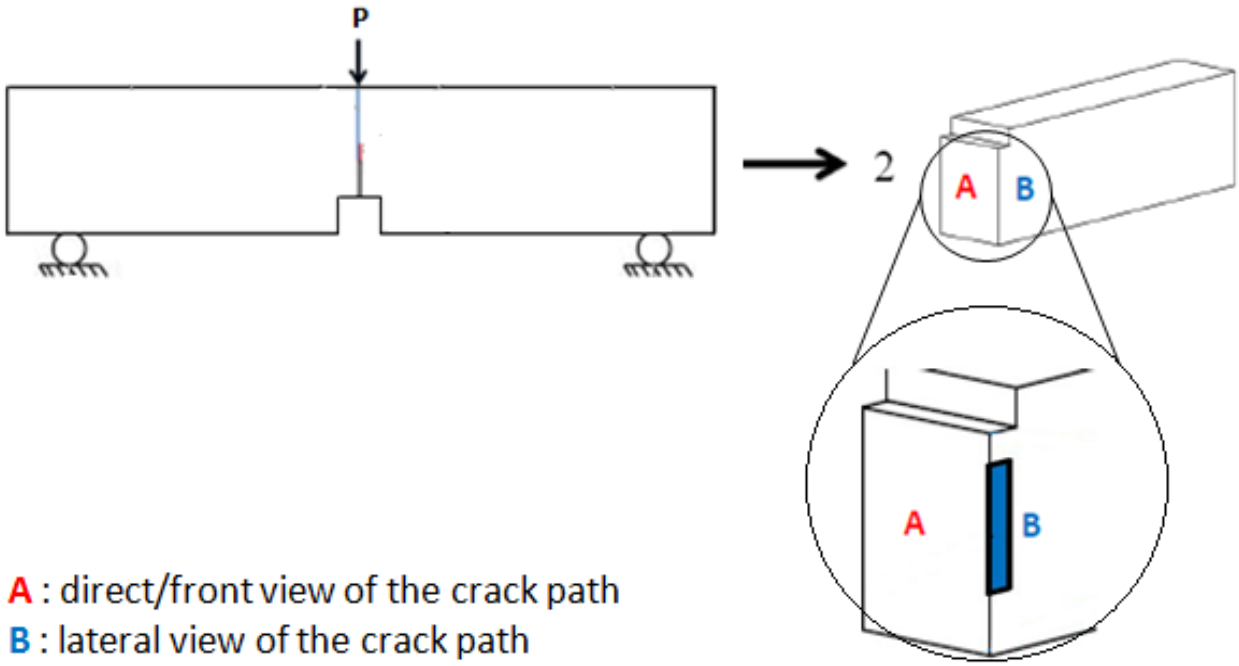

Figure 4. Description of the orientation and positioning of the two fracture surface views characterized by SEM and optical microscopy for the SENB specimens with a TS-TP interphase.

3. RESULTS AND DISCUSSION

3.1 Microstructure of the homogenous blends

Figure 5 shows optical micrographs of the microstructure corresponding to homogenous blends with (a) 90-10 % RTM6-PEI, (b) 85-15 % RTM6-PEI and (c) 75-25% RTM6-PEI. In the 10% PEI range, a sea-island morphology is observed with small PEI rich regions in a RTM6 sea. In the 25% PEI range, the phase inversion occurred with a RTM6 rich nodular morphology surrounded by a continuous PEI rich layer. The 15% PEI content leads to a co-continuous morphology. As explained in [60], the sea-island and nodular morphologies correspond to a quasi-equilibrium situation after full phase separation dominated by interfacial energy as can be predicted with a phase field type model. However, the tortuous co-continuous microstructure can only be understood by invoking viscoelastic effects, more precisely a large difference in viscoelastic behaviour between the two phases, which modifies the usual interfacial energy dominated morphology development, following the concept of viscoelastic phase

separation pioneered by H. Tanaka, see ref [61-62] and references therein.

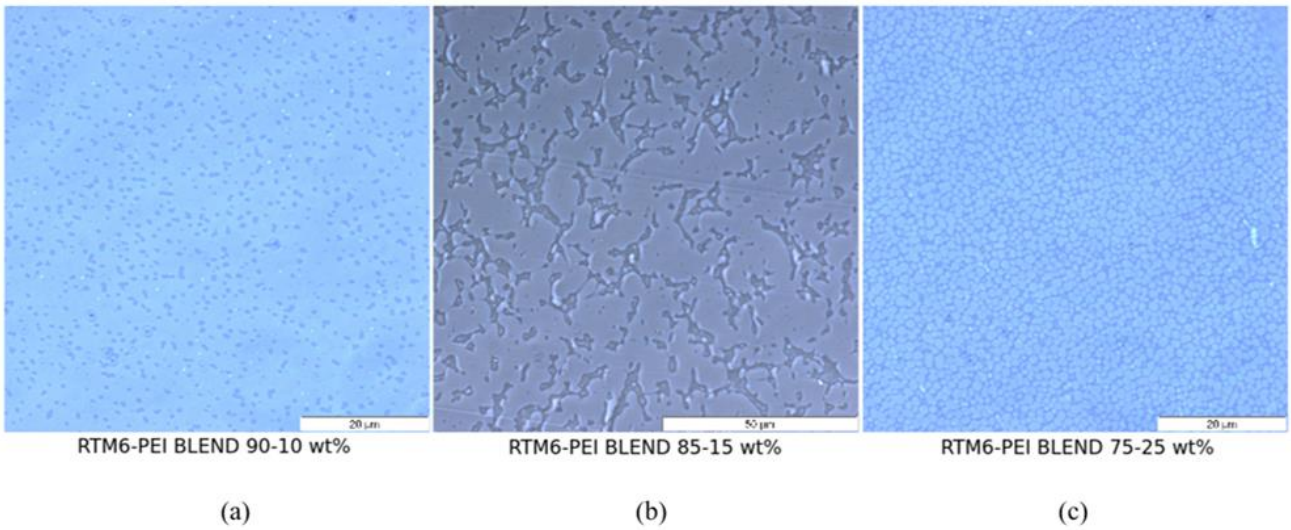

Figure 5. Optical microscopy micrographs of three different RTM6-PEI blends: with (a) 10%, (b) 15% and (c) 25 wt% of PEI representative of the sea-island, co-continuous and nodular morphology, respectively.

3.1. Elastoplastic properties of homogenous RTM6-PEI blends

The elastoplastic response of the blends 100-0, 95-5, 85-15, 0-100 (%RTM-%PEI) was extracted from uniaxial compression tests. Figure 6 shows the true stress – true strain curves with a zoom on the region around the onset of plasticity. The dispersion in the stress-strain responses for each replicate of the same material is smaller than the differences between the different systems giving confidence to a quantitative comparative analysis. The elastic moduli are slightly below the expected values: E_{RTM6} = ~2.3 GPa and E_{PEI} = ~2 GPa while the nominal values are around 3 GPa for both polymers. This difference is due to the absence of correction for the machine compliance in the treatment of the data. This does not significantly influence the results at larger strains and does not affect the magnitude of the reported stress values, nor the discussion to come which focus on the strength and not on the material stiffness.

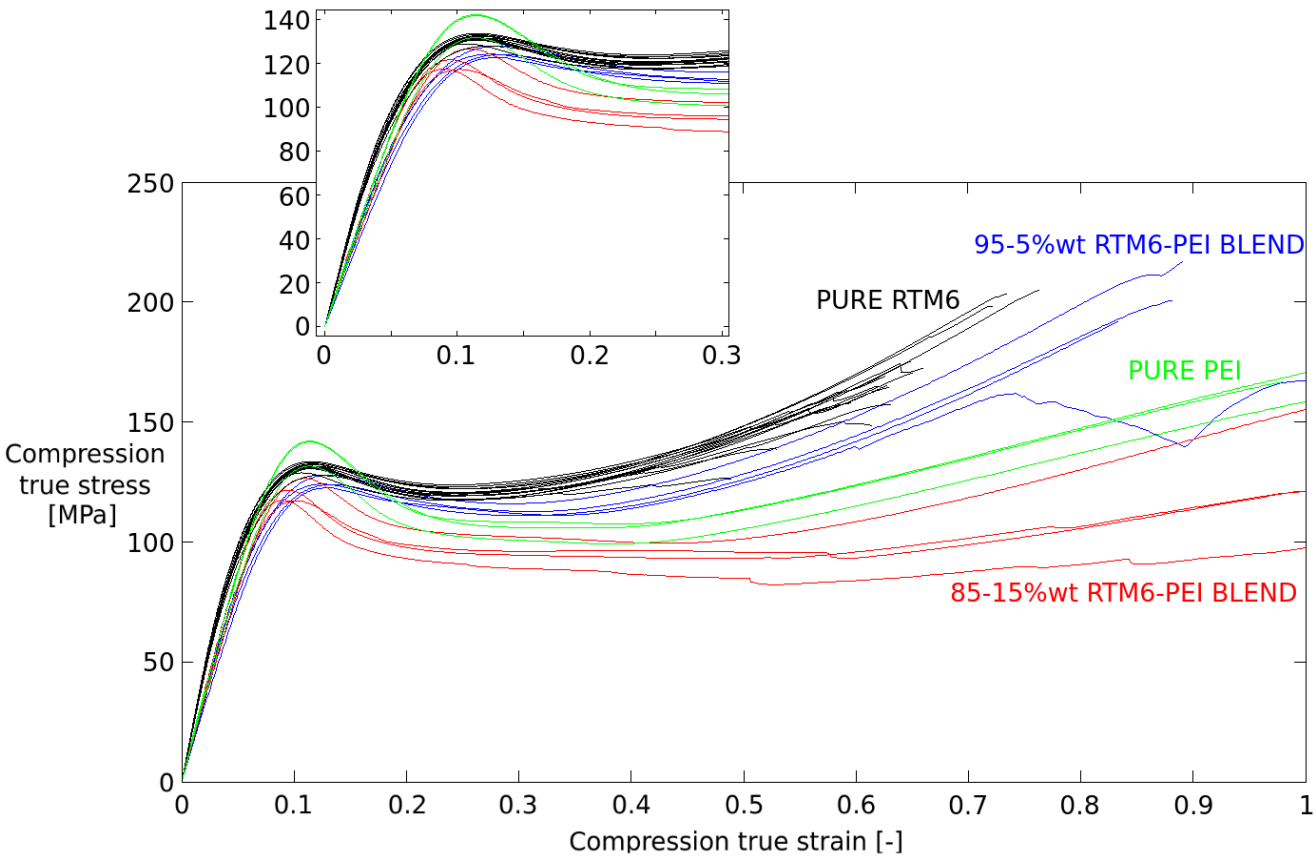

Figure 6. True stress-true strain curves corresponding to the uniaxial compression of homogenous RTM6-PEI blends at a constant crosshead displacement rate of 1 mm/min. The zoom provides a magnified view of the zone near the onset of plasticity.

The most important result emerging from Figure 6 is that the 85-15 RTM6-PEI blend exhibits the lowest strength in compression. As the exact determination of the onset of plasticity in a complicated matter, requiring systematic loading/unloading sequences near the stress peak, we assume here that the peak value reflects the resistance of the polymer to the beginning of plasticity. The peak strength is attained at a strain of about 0.1. All systems exhibit significant post-peak softening, and it is also interesting to report the lower yield stress value. Figure 7 shows the variation of the high (peak) and low yield stress as a function of PEI content. The dotted line is a simple interpolation of the data points. The peak yield stress of PEI is slightly higher than RTM6 (≈140 MPa vs. ≈130 MPa) while the opposite trend is found for the lower yield stress (PEI≈110 MPa vs. RTM6≈120 MPa). The PEI shows thus a larger softening. The 85-15 RTM6-PEI blend exhibits significantly smaller peak strength and lower

yield stress compared to the other systems. The re-hardening capacity of the 85-15 RTM6-PEI blend is also very limited. The strength RTM6-PEI system does thus not follow the simple rule of mixture but exhibits a softening effect upon mixing.

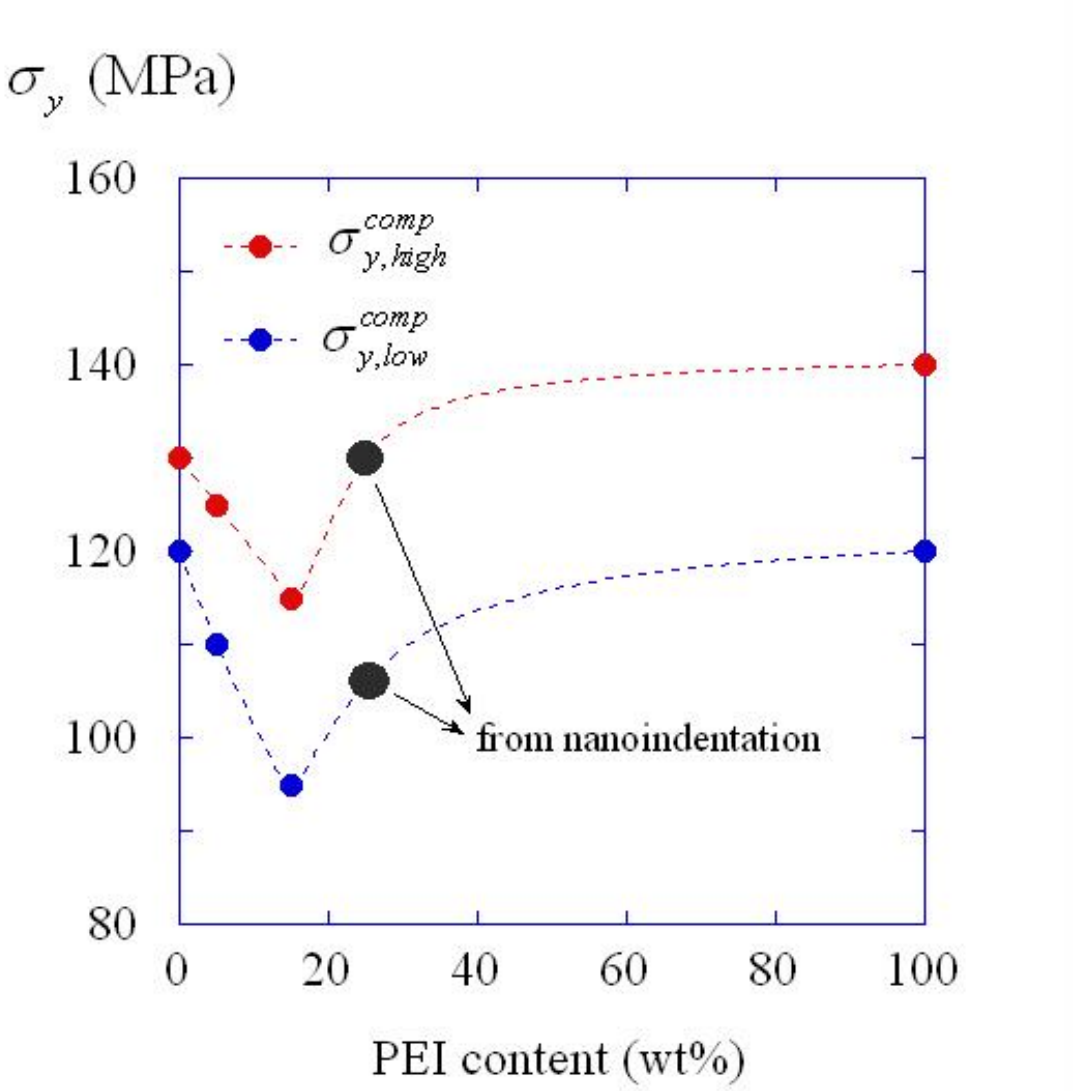

Figure 7. Variation of peak strength and lower yield stress as a function of the PEI content for homogenous blends and pure systems; the point at 25% PEI content is obtained from nanoindentation data and the method explained in the text.

In order to consolidate the finding that homogenous blends show a minimum strength at intermediate PEI content, nanoindentation tests are performed on the different systems, involving the 75-25 % RTM6-PEI blend for which no macroscopic compression specimens could be processed. First, the elastic modulus, extracted using the Oliver and Pharr method [58] remains in the same range of ~4 GPa

from 3.9 GPa for RTM to 4.3GPa for pure PEI (not shown). Note that a higher modulus is very often found by nanoindentation in polymers when compared to values obtained with macroscopic tests for reasons that are not yet fully clarified [63]. Figure 8a shows the variation of the hardness as a function of PEI content with the dashed line being the interpolation between the data points proposed as eye-guides. The hardness H can be related to the yield stress σ_y through the proportionality factor α. The value of α for a perfectly plastic von Mises material is close to 3, but it is known to vary with the pressure sensitivity, E/σ_y ratio and strain hardening exponent [63-64]. Generally, α is smaller than 3 in polymers [65]. Figure 8b shows the evolution of α with increasing PEI content: α_{high} and α_{low} represent the factors giving the best match with the upper and lower yield stress values, respectively. The interest of determining α is to convert nanoindentation hardness into yield stress for intermediate compositions. The best match α_{high} is close to 2.4 almost over the entire composition window. This is slightly lower than the ratio obtained for PEEK, high-density polyethylene and PMMA [63,65] and slightly higher than in polystyrene, polycarbonate or polyamide 12 [63,65]. On the other hand, the variation of α_{low} is more pronounced as it increases from 2.8 for RTM6 to 3.1 for pure PEI, which is closer to the classical value $\alpha = 3$. This analysis shows that the 75-25 % RTM6-PEI blend would exhibit a peak (high) yield strength of about 130MPa as added to Figure 8a, confirming a local minima for PEI content around 15%.

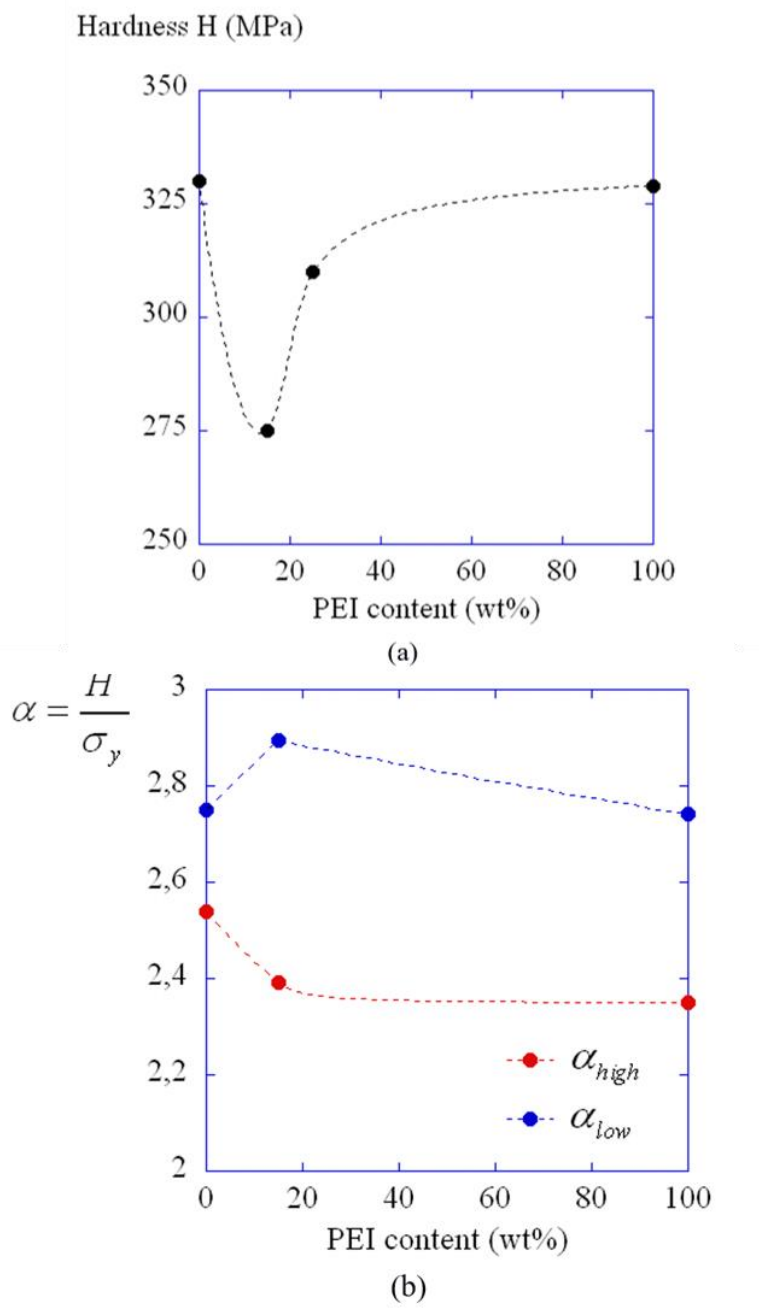

Figure 8. Variation as a function of PEI content of (a) the nanoindentation hardness and of the (b) proportionality factors α_l and α_u linking lower and peak yield stress to hardness.

The origin of the softer behaviour of the 85-15% PTM6-PEI composition requires more discussion, as it will have a major impact on the fracture resistance (see next sections). First, there is no doubt about the lower strength of this composition: the peak stress in compression is the lowest, the hardness is the lowest and the re-hardening capacity measured in compression is also the lowest.

In Figure 5(b), the 85-15% PTM6-PEI composition exhibits a co-continuous morphology. This co-continuous morphology is related to a viscoelasticity dominated phase separation process as already explained above. The microstructure is thus very far from equilibrium, with significant amount of excess energy. The excess energy appears in the form of residual stress, extra free volume, and local stress concentration associated to the very distorted morphology. Based on the current understanding of the mechanisms dictating the viscoplastic behaviour of thermosets and thermoplastics, a rejuvenated state associated to heterogeneous excess energy landscape is known to favour, through mechanical energy contribution, the activation of molecular rearrangements, related also to so-called β transformation. Recently, the shear transformation zone formalism, which is a continuum mechanics description of these molecular atomistic configuration changes, has been found highly relevant to predict the viscoplastic response of epoxies [66]. In particular, rejuvenated states were found to decrease the strength and increase the creep rates through decreasing the barrier for these transformations due to local stress heterogeneities (also called back-stress). These explanations require more advanced modelling and nanomechanical testing for validation, which is left for future works as the goal of the present study is focused on the fracture resistance of the PEI/RTM6 interphase region.

3.3 Fracture resistance of TS-TP interphases

Figure 9 presents the results from the three-point bending cracking tests performed on the RTM6-PEI interphases in terms of the initiation fracture toughness G_{Ic} as a function of the curing cycle (see Section 2.4). The values for the pure materials are also included as reference points. Both C_{160} and C_{180}-cured systems present similar high values of G_{Ic} (~800 J/m²) falling in the range typical of good structural adhesives used in aeronautics, which is an excellent (and initially unexpected) result. This value is almost five times larger than the bulk RTM6 one. By contrast, the $C_{180,slow}$-cured system has a lower toughness with a significantly lower mean G_{Ic} (~400 J/m²) but still more than two times higher than the pure RTM6 fracture toughness. The dispersion on these results is larger than for the two other systems.

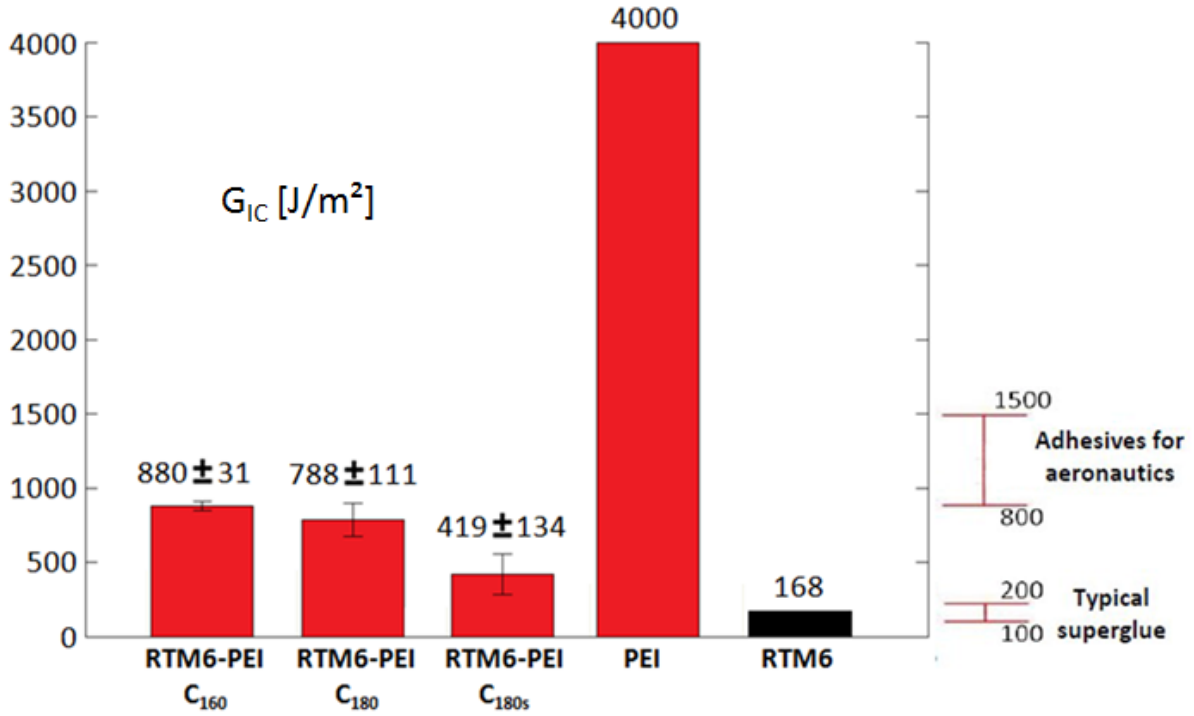

Figure 9. Variation of the fracture toughness G_{Ic} of the RTM6-PEI interphase as a function of the curing cycle. Fracture toughness values for the neat references are also shown.

The morphological gradients inside the interphase regions are investigated on lateral cross-sections by phase contrast optical microscopy in order to provide a first qualitative understanding of the origin of the difference in fracture resistance between the $C_{180,\ slow}$-cured RTM6-PEI and both C_{160} and C_{180}-cured RTM6-PEI systems, see Figure 10. Both C_{160} and C_{180}-cured RTM6-PEI (Figures 10a and 10b) show a similar morphology characterized by the presence of an extensive PEI nodular phase on the RTM-rich side of the interdiffusion zone, which can be swollen by typical PEI solvents, and by the presence of a co-continuous region spreading over 8-10 μm thickness between the PEI-rich and RTM6-rich zones.

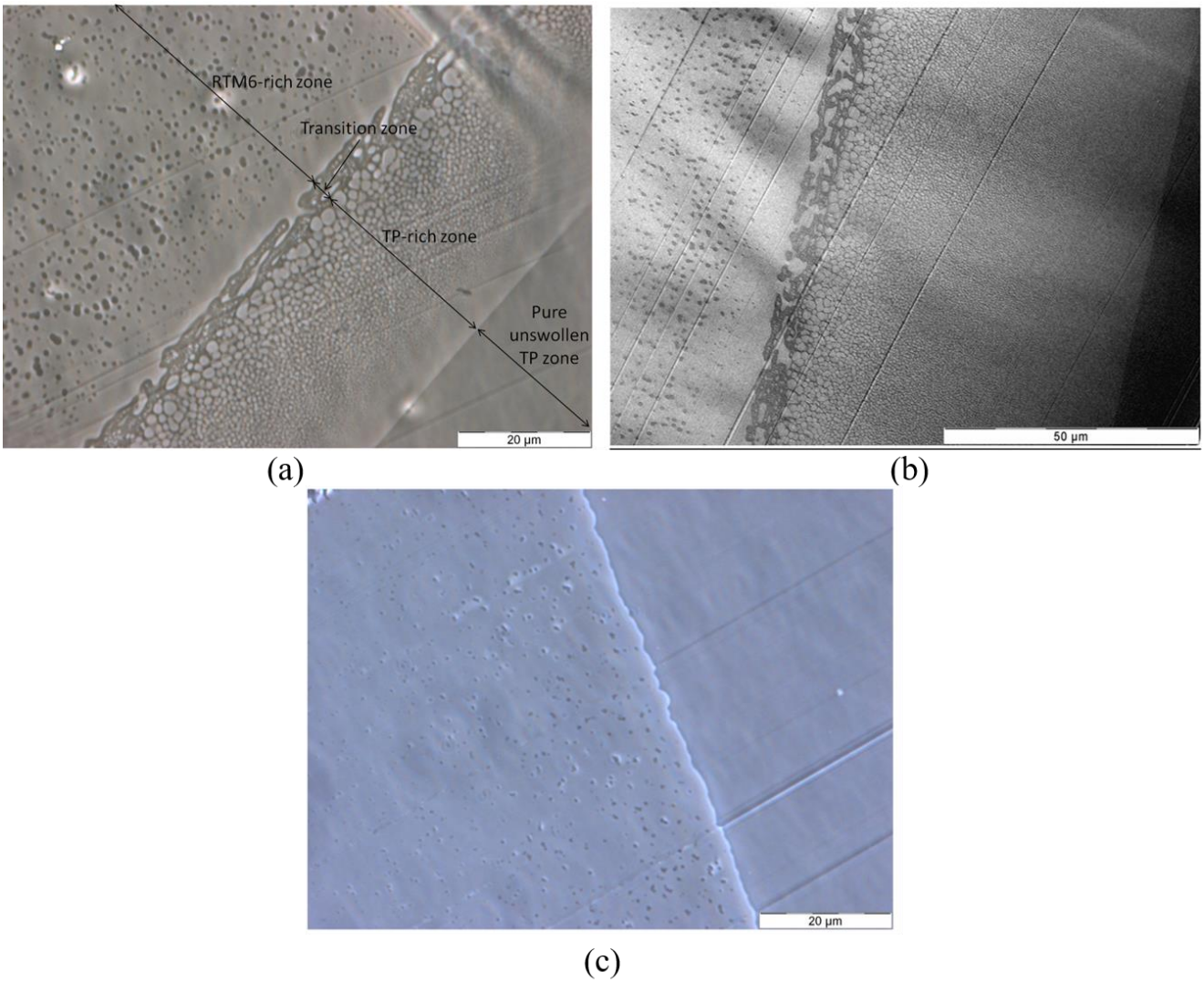

Figure 10. Optical microscopy micrographs of the morphological gradient associated to (a) the C_{180}-cured RTM6-PEI interphase, (b) the $C_{160\text{-cured}}$ RTM6-PEI interphase and (c) the $C_{180,slow}$-cured RTM6-PEI interphase. The dark and light phases correspond to the PEI-rich and RTM6-rich phases, respectively.

On the other hand, in the $C_{180,slow}$-cured RTM6-PEI interphase does not present any swelling zone if the slice is brought in contact with a PEI solvent and does not show any sign of a PEI nodular morphology on the RTM-rich side nor any co-continuous transition zone (see Figure 10c). This is indicative of a sharp RTM6-PEI interface and a clear hint towards a lower potential for triggering toughening mechanisms during crack propagation.

The next step is to determine where the crack propagates. As illustrated in Figures 11 to 15 taken from both front and lateral views (“A” and “B” in Figure 4), the crack is always trapped in the

morphological gradient zone during its propagation for the C_{160} and C_{180}-cured RTM6-PEI systems. This trapping mechanism is the core finding of this study. Three different failure mechanisms are observed. The first mechanism manifests itself in the form of a zig-zag crack pattern in the PEI-rich region between the RTM6-PEI transition zone and the boundary separating the nodular and pure PEI zones. These oscillations can be observed on the front views ("A") of fracture surfaces by a crack meandering path such as the one shown in Figure 11.

The two other mechanisms are illustrated in Figures 12 and 13. They correspond to the limiting cases of the first one, i.e. the localized propagation of the crack either in the PEI-rich region close to the boundary separating the swellable and pure PEI zones or in the RTM6-PEI transition zone. The second mechanism is characterized by the leaves-like structure shown in Figure 12. The front view of a fracture surface corresponding to the third mechanism is illustrated in Figure 13. The lateral view ("B") of the fracture surface of a C_{160}-cured RTM6-PEI interphase is shown in Figure 14 and summarizes these three crack confinement type behaviors from a different point of view.

In contrast, there is no morphological feature allowing the crack to be trapped in the $C_{180,slow}$-cured RTM6-PEI interphase. Here, the crack propagates either in the RTM6-rich region of the interphase or follows the sharp interface at the RTM6-PEI transition zone, as seen in Figure 15.

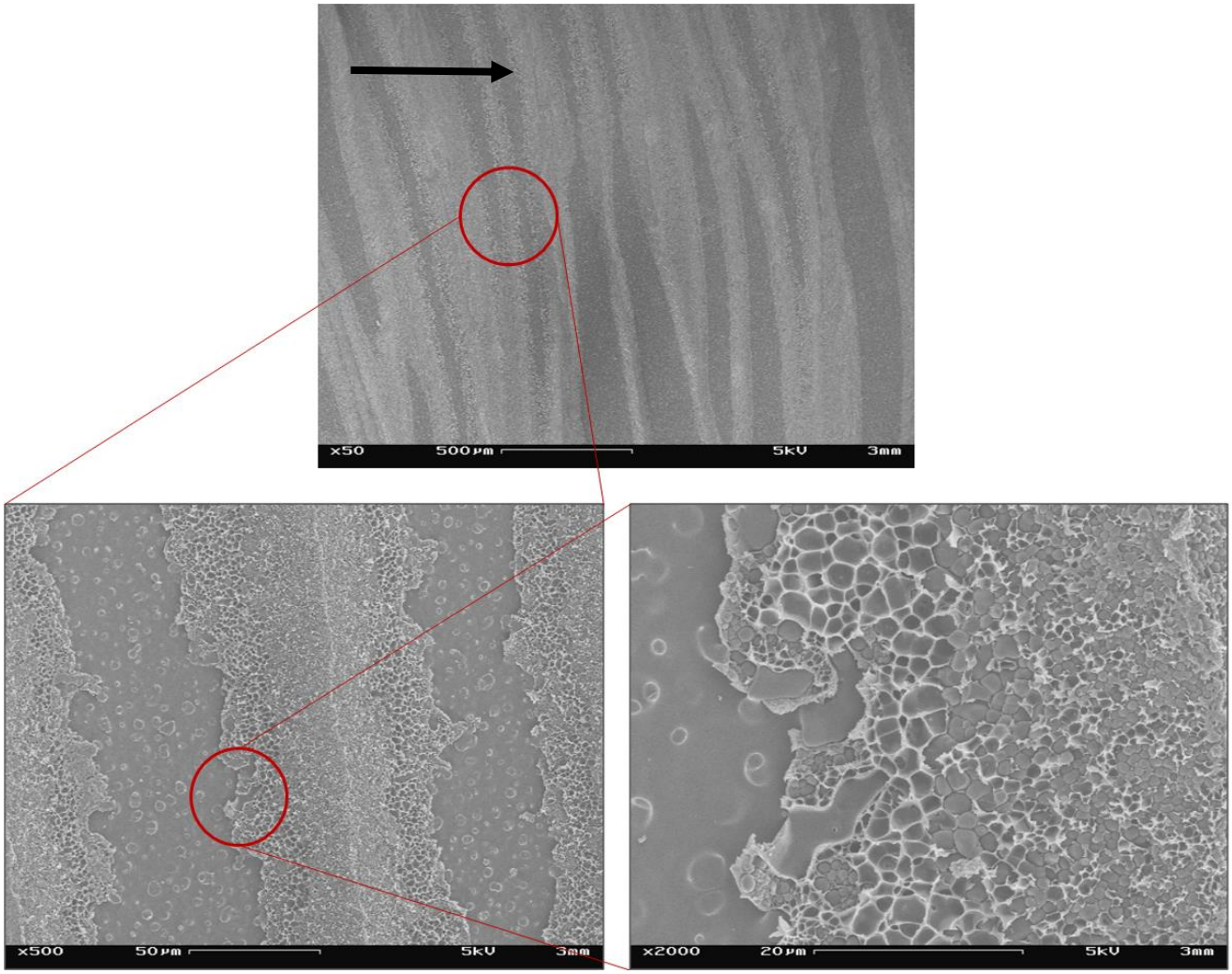

Figure 11. SEM front view micrographs of the fracture surface from a broken SENB specimen in the case of the C_{160}-cured RTM6-PEI system: crack meandering patterns in the PEI-rich zone. The arrow indicates the direction of crack propagation.

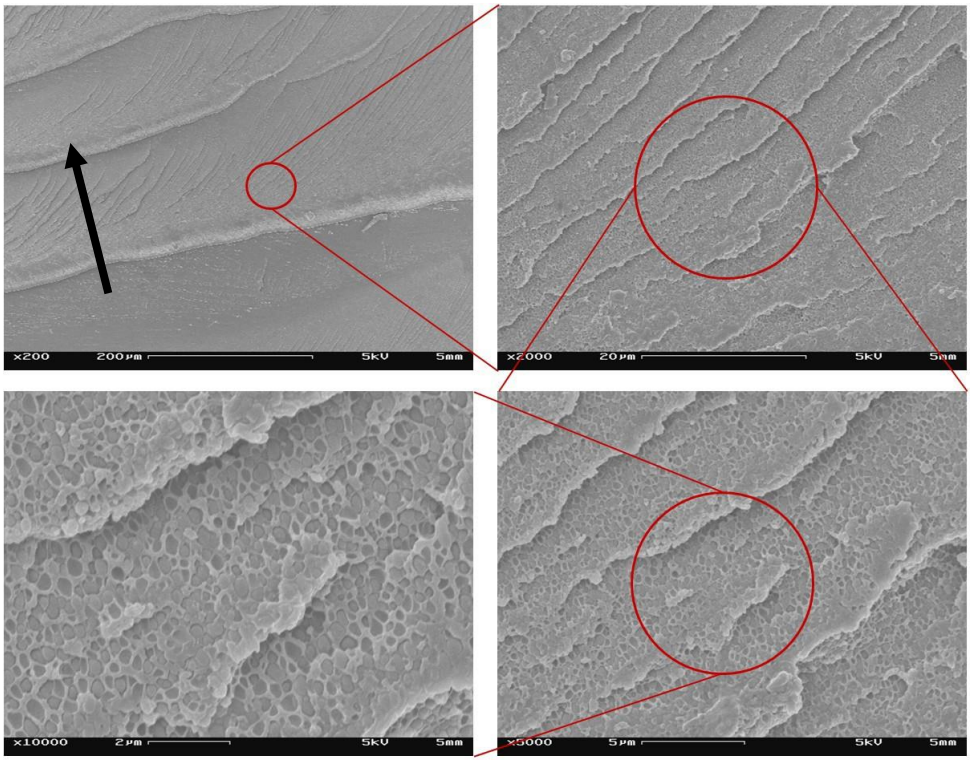

Figure 12. SEM front view micrographs of the fracture surface from a broken SENB specimen in the case of the C_{160}-cured RTM6-PEI system: leaves-like patterns. The arrow indicates the direction of crack propagation.

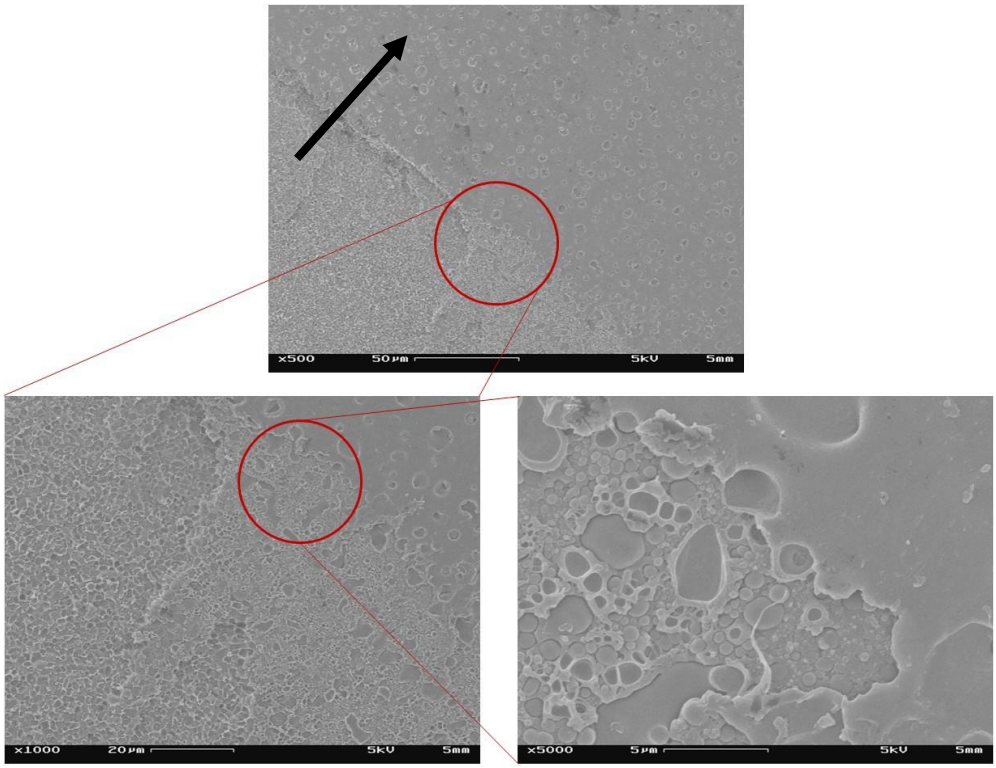

Figure 13. SEM front view micrographs of the fracture surface from a broken SENB specimen in the case of the C_{160}-cured RTM6-PEI system: crack propagating in the transition zone. The arrow indicates the direction of crack propagation.

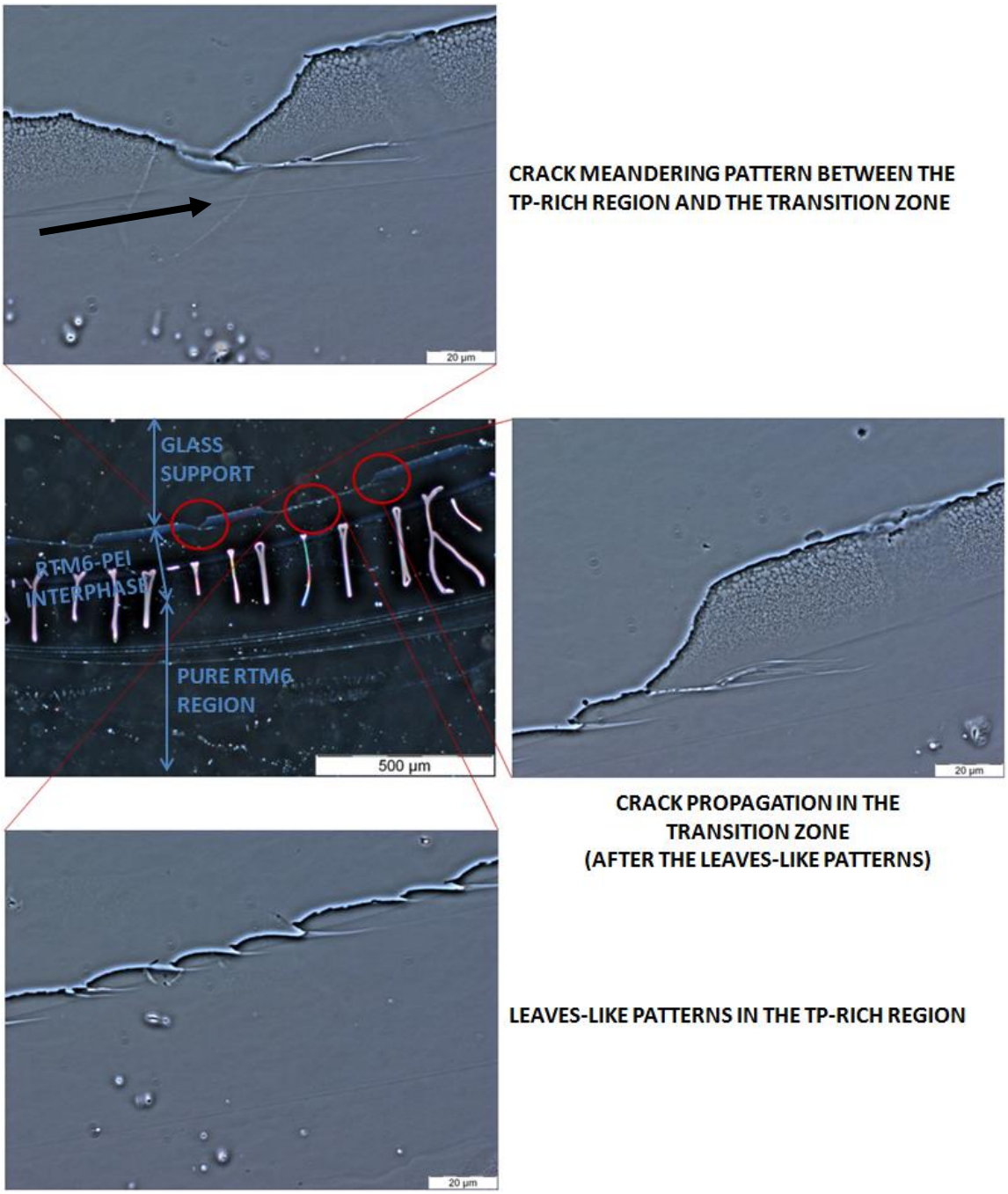

Figure 14. Optical microscopy lateral views of the fracture surface from a broken SENB specimen in the case of the C_{160}-cured RTM6-PEI system: summary of the different crack propagation features observed from the front views. The arrow indicates the direction of crack propagation.

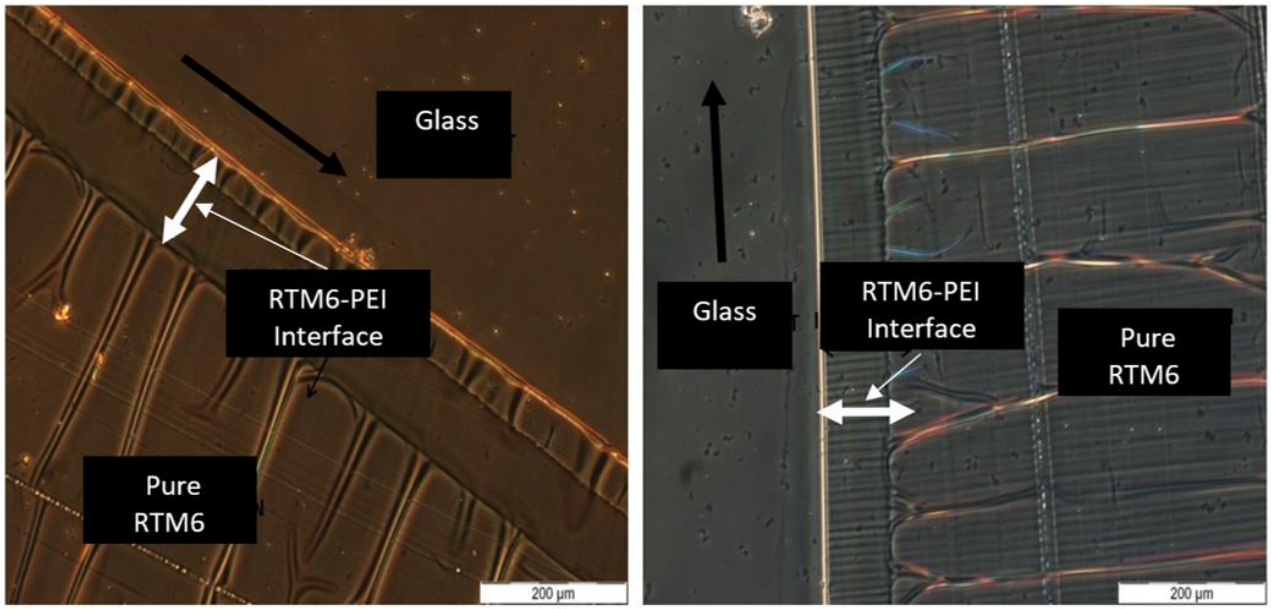

Figure 15. Optical microscopy lateral views of the fracture surface from a broken SENB specimen in the case of the $C_{180,slow}$- cured RTM6-PEI system: the crack propagates in the RTM6-rich region of the interphase (left) or follows the sharp interface defining the RTM6-PEI transition zone (right).

A representation is provided in Figure 16 in order to schematize all the crack path scenarios found in the interdiffusion zone.

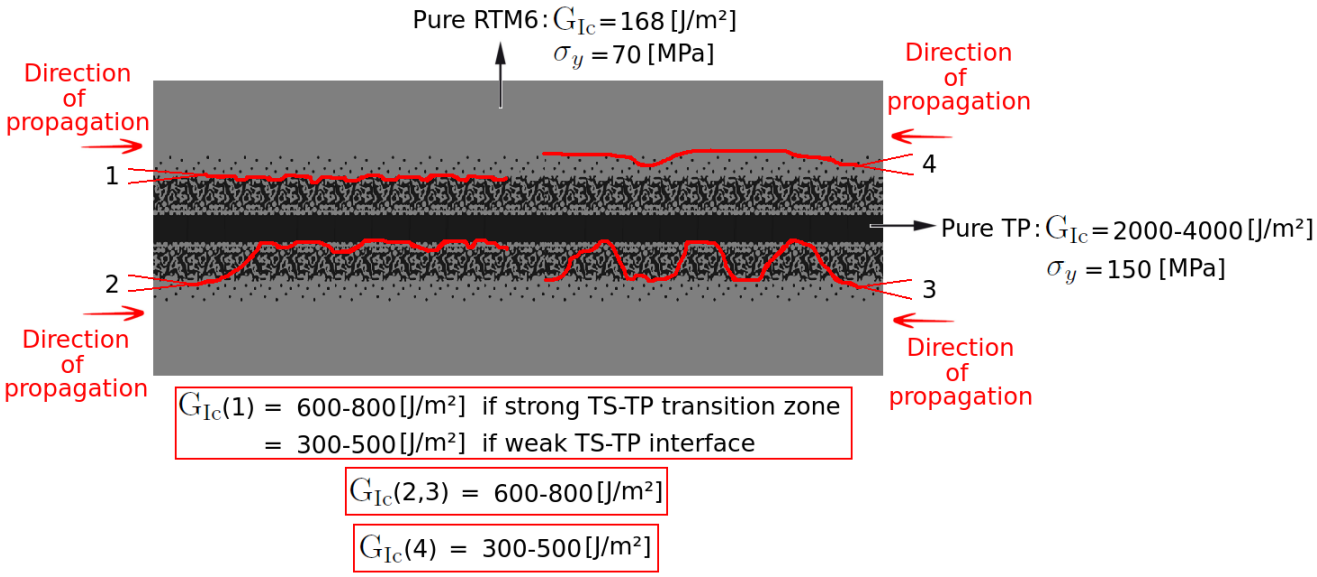

Figure 16. Schematics of the different scenarios of crack propagation depending on whether the interphase exhibits a tough or a brittle behavior.

3.4 Discussion on the origin of the interface toughening by crack trapping

Based on the results presented above, the difference in fracture toughness between both C_{160} and C_{180}-cured systems and the $C_{180,slow}$-cured system can thus be qualitatively attributed to differences in the morphology of the corresponding interphases leading to the trapping of the crack inside a softer but tougher region. The main factor discriminating the two types of systems is the presence or not of a broad transition zone between the PEI-rich and RTM6-rich regions with an interpenetrated co-continuous morphology spreading over 8-10 μm thickness, which enables mechanical interlocking (compare Figures 11-13 and 14). Moreover, this difference is in turn strongly related to the confinement or not of the crack propagation process within the interfacial zone.

The key question is why the crack remains trapped in the interphase region and does not kink within the much more brittle RTM6 material? Figure 17 shows the schematic evolution of the fracture toughness and of the yield stress inside the interphase. Based on these variations, the following scenario can be proposed and substantiated. Once the crack propagates in the TP-rich region of the interphase - for instance due to a deviation coming from a defect or due to a slight angle mismatch in the test set up or to the development of an asymmetric loading of the specimen during the fracture process - it is either blocked on the pure PEI side by a fracture toughness barrier or inside the transition zone side by a lower yield stress. In other words, once trapped in the TP-rich region, which involves a relatively high toughness, the crack cannot cross the pure PEI because the fracture toughness is there even higher. Moreover, as the crack experiences a change of direction when approaching the pure PEI boundary, the propagation occurs at an angle with respect to the direction of the loading, which introduces a mode II contribution, hindering even more its progression. On the other hand, the crack cannot go through the transition zone towards the RTM6 rich side either because the strength around is larger.

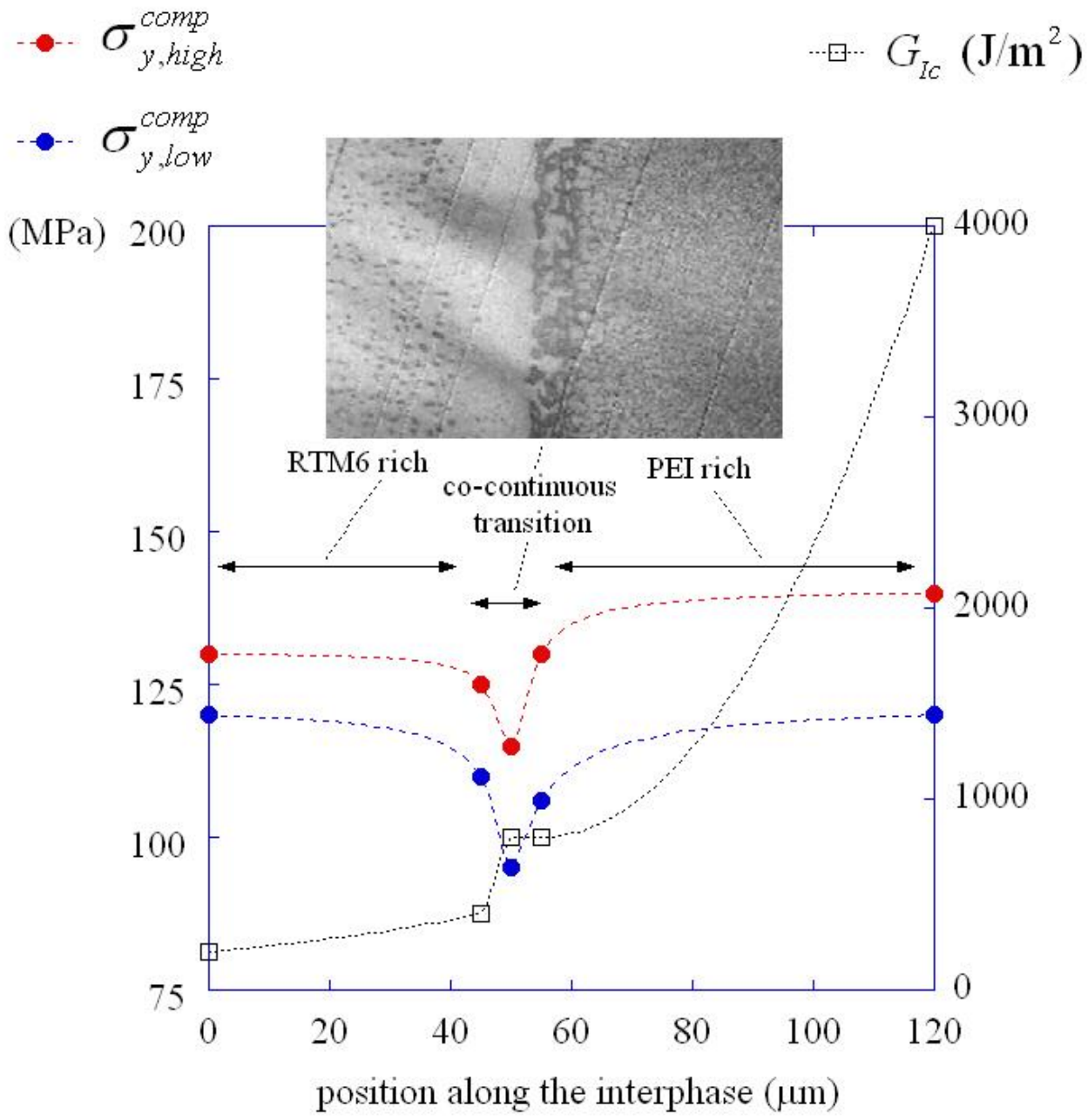

Figure 17. Semi-quantitative evolution across the thickness of the morphological gradient of a C_{160} or C_{180}-cured RTM6-PEI interphase of the critical energy release rate and yield stress, explaining the crack trapping mechanism and resulting interface toughening.

This interesting result reminds us that the crack trajectory in heterogeneous systems is not determined by the local fracture resistance only but also very much by the local strength level. This working principle opens the doors to the design of joints with high cracking resistance if one can prepare systems/interphases with soft-and-tough intermediate compositions or with soft-and-tough interlayers.

Here, again, the existence of soft-and-tough composition, near 15% PEI, is related to a co-continuous morphology, which was already known to provide good toughness by forcing the crack to cross the tough PEI zones. However, a novel aspect in this study was the significantly lower strength of this intermediate composition, tentatively connected to a far out of equilibrium structure similar to a rejuvenated state. This aspect requires additional investigation to confirm and further exploit this finding.

CONCLUSION

The morphological characteristics and mechanical behavior - elasto-plasticity as well as fracture resistance- of RTM6 – PEI interdiffused systems have been studied as a prototypical model of interphases found in high performance thermoset-thermoplastic jointly cured structures. We have observed that the two aspects of local morphology and local properties are highly interlinked, leading to a remarkable fracture toughness associated to the presence of a broad interlocked interphase with smooth TS-TP concentration gradient. This gradient favors the interfacial confinement of the cracks within a softer but high toughness domain with low TP content. Some specific findings are summarized below:

- The results from uniaxial compression tests and nanoindentation experiments on homogeneous blends give consistent evidence of a softening effect upon mixing RTM6 and PEI at around 15% PEI content.
- The results from three-point bending tests with pre-cracks located on the interphases show that for “fast” curing cycles, RTM6-PEI interphases exhibit reproducible initiation fracture toughness values of the same order of magnitude as high performance structural adhesives, hence validating their potential use in aeronautical applications; the opposite is found “slow-cured” systems, within the limit of our experimental data.
- The observed toughening can be explained by the combination of a broad interfacial zone including a co-continuous morphology region at low PEI content with softer but tougher behavior compared

to the neat RTM6 reference. This leads to the trapping of the propagating cracks in or near the TP-rich regions and to a high joint toughness. By contrast, brittle interfaces are associated to the propagation of the crack inside the RTM6-rich region or at the sharp transition zone between TP-rich and RTM6-rich regions.

While it would be very attractive to analyze in situ the "softening layer" of real interfaces, this is unfortunately not feasible, at least not with nanoindentation. In Figure 11 of ref [55] it can be checked that the concentration gradient is very steep, even for broad interfaces, of the order of 15-20% per micron across the interphase. Since the softening concentration range extends only over 10% at most (see Figure 9 of the present work), it would require submicron resolution to identify the softened region. More realistically, the use of numerical methods for the simulation of crack propagation through TS-TP interphases would bring a helpful contribution to the further understanding of the damage/toughening mechanisms of these systems and are in this sense a clear perspective to this work. Crack trapped within soft regions of welded or bonded joints has obviously been observed prior to this work, but generally leading to a reduction of the joint performance. The novelty here is that it leads to very significant toughening because of the local high cracking resistance of the co-continuous morphology. There is much room to systematize and tailor this concept in TP/TS interfaces. Numerical methods, in the spirit for instance of Ref [67], could indicate what is the ultimate toughening that could potentially be attained and guide system optimization.

ACKNOWLEDGMENTS

Q. V. gratefully acknowledges the support of FNRS/FRIA PhD grant. The work has also been carried out under the umbrella of the SKYWIN (Wallonia) project ECOTAC.

REFERENCES

[1] Zweben C. *Advanced composites for aerospace applications – a review of current status and future prospects*. **Composites**, 1981, 12: 235–40.

[2] Soutis C. *Fibre reinforced composites in aircraft construction*, **Prog Aerosp Sci**, 2005, 41:143–51.

[3] Harris CE, Starnes JH, Shuart MJ. *An assessment of the state-of-the-art in the design and manufacturing of large composite structures for aerospace vehicles* [NASA/TM-2001-210844].

[4] Marsh G. *Airbus takes on Boeing with reinforced plastic A350 XWB. In: Reinforced plastics*, **Elsevier Ltd.**, 2007.

[5] Kaufmann M, Zenkert D, Wennhage P. *Integrated cost/weight optimization of aircraft structures*, **Struct Multidiscip Opt**, 2009, 41(2):325–34.

[6] Curran R, Chou S-Y, Trappey A, Mullen M, Brolly N, Gilmour M, et al. *Modelling of aircraft manufacturing cost at the concept stage*, **Int J Adv Manuf Technol**, 2006, 31(3–4):407–20.

[7] Hart-Smit LJ. Further developments in the design and analysis of adhesive bonded structural joints. In: Kedward KT, editor. A symposium sponsored by ASTM committee D-30 on high modulus fibers and their composites, vol. 749. Minneapolis (Minn.): ASTM Special Technical Publication; 1980.

[8] Higgins A. *Adhesive bonding of aircraft structures*. **Int J Adhes Adhes**, 2000, 20: 367–76.

[9] Ashcroft IA, Hughes DJ, Shaw SJ. *Adhesive bonding of fibre reinforced polymer composite materials*, **Assembly Automation**, 2000, 20(2):150–61.

[10] Thoppul SD, Finegan J, Gibson RF. *Mechanics of mechanically fastened joints in polymer–matrix composite structures – a review*. **Compos Sci Technol**, 2009, 69(3–4):301–29.

[11] Banea MD, da Silva LFM. *Adhesively bonded joints in composite materials: an overview*, **Proc Inst Mech Eng Part L: J Mater Des Appl**, 2009.

[12] Adams RD, Comyn J. *Joining using adhesives*, **Assembly Automation**, 2000, 20(2): 109–17.

[13] Hou M. *Thermoplastic adhesive for thermosetting composites*, **Quebec City (QC, Canada): Trans Tech Publications Ltd**, 2012.

[14] Hou M. *Fusion bonding of carbon fibre reinforced epoxy laminates*, **Penang (Malaysia): Trans Tech Publications**, 2013.

[15] Wedgewood AR, Hardy PE. *Induction welding of thermoset composite adherends using thermoplastic interlayers and susceptors*, **In: Proceedings of the 28th international SAMPE technical conference**, Seattle (WA, USA), November 4–7 1996.

[16] Ageorges C, Ye L, Hou M. *Advances in fusion bonding techniques for joining thermoplastic matrix*

composites: a review, **Composite part A Appl Sci Manuf**, 2001, 32(6): 839–57.

[17] Yousefpour A, Hojjati M, Immarigeon J-P. *Fusion bonding/welding of thermoplastic composites*, **J Thermoplast Compos Mater**, 2004, 17(4): 303–41.

[18] Don RC, McKnight SH, Wetzel ED, Gillespie JW Jr. *Application of thermoplastic resistance welding techniques to thermoset composites*, **In: Proceedings of the 52nd annual technical conference ANTEC 94**, Part 1 (of 3), May 1–5 1994. San Francisco, CA, USA. Brookfield (CT, USA): Publ by Soc of Plastics Engineers.

[19] Beehag A, Falzon P, Paton R. *A mouldable thermoplastic interface for advanced composite components to reduce costs in aircraft assembly*, **In: SAE technical paper at aerospace technology conference and exhibition**, 2005.

[20] Paton R, Hou M, Beehag A, Falzon P. *A breakthrough in the assembly of aircraft composite structures*, **In: 25th international congress of the aeronautical sciences**, 2006.

[21] Tian Zhao, Calvin Rans, Irene Fernandez Villegas, Rinze Benedictus. *On sequential ultrasonic spot welding as an alternative to mechanical fastening in thermoplastic composite assemblies: A study on single-column multi-row single-lap shear joints*, **Composite Part A: Applied Science and Manufacturing**, 120, 2019: 1-11.

[22] Tian Zhao, Charlotte Broek, Genevieve Palardy, Irene Fernandez Villegas, Rinze Benedictus. *Toward robust sequential ultrasonic spot welding of thermoplastic composites: Welding Process Control strategy for consistent weld quality*, **Composite Part A**, 2018, 109: 355-367.

[23] Irene Fernandez Villegas, Pablo Vizcaino Rubio. *On avoiding thermal degradation during welding of high-performance thermoplastic composite to thermoset composite*, **Composite Part A: Applied Science and Manufacturing**, 77, 2015: 172-180.

[24] H. Shi, I.F. Villegas, H.E.N. Bersee. *A displacement-detection based approach for process monitoring and processing window definition of resistance welding of thermoplastic composites*, **Composite Part A: Applied Science and Manufacturing**, 74, 2015:1-9.

[25] Genevieve Palardy, Huajie Shi, Arthur Levy, Steven Le Corre, Irene Fernandez Villegas. *A study on amplitude transmission in ultrasonic welding thermoplastic composite*, **Composite Part A: Applied Science and Manufacturing**, 113, 2018: 339-349.

[26] Francesca Lionetto, Maria Nicolas Morillas, Silvia Pappada, Giuseppe Buccoliero, Irene Fernandez Villegas, Alfonso Maffezzoli. *Hybrid Welding of carbon-fiber reinforced epoxy based composites*, **Composite Part A: Applied Science and Manufacturing**, 104, 2018: 32-40.

[27] Irene Fernandez Villegas, Regis van Moorleghem. *Ultrasonic welding of carbon/epoxy and*

carbon/PEEK composites through a PEI thermoplastic coupling layer, **Composite Part A: Applied Science and Manufacturing**, 109, 2018, 75-83.

[28] Jose Angel Ramos, Miren Blanco, Inaki Zalakain, Inaki Mondragon. *Nanoindentation study of interphases in epoxy/amine thermosetting systems modified with thermoplastics*, **Journal of Colloid and Interface Science**, 336, 2, 2009: 431-437.

[29] Shiqiang Deng, Luke Djukic, Rowan Paton, Lin Ye. *Thermoplastic-epoxy interactions and their potential applications in joining composite structures-A review*, **Composite Part A: Applied Science and Manufacturing**, 68, 2015: 121-132.

[30] Ebnesajjad C. Theories of adhesion. In: Ebnesajjad C, editor. *Surface treatment of materials for adhesive bonding*, **Elsevier Science**, 2013.

[31] Petrie EM. *Theories of adhesion*, **Handbook of adhesives and sealants**, McGraw-Hill, 2000.

[32] Allen KW. *Some reflections on contemporary views of theories of adhesion*, **Int J Adhes Adhes**, 1993, 13(2): 67–72.

[33] Allen KW. *A review of contemporary views of theories of adhesion*, **J Adhes**, 1987, 21:261–77.

[34] Kinloch AJ. *Mechanisms of adhesion*, **Adhesion and Adhesives: Science and Technology**, Chapman and Hall, 1987.

[35] Kamme HW. *Adhesion between polymers*, **Acta Polym**, 1983, 34: 112–8.

[36] Comyn J. *Introduction to adhesion and adhesives*, Adhesion Science, **The Royal Society of Chemistry**, 1997.

[37] Wake WC. *Theories of adhesion and uses of adhesives: a review*, **Polymer**, 1978, 19:291–308.

[38] Fourche G. *An overview of the basic aspects of polymer adhesion. Part I: Fundamentals*, **Polym Eng Sci**, 1995, 35(12):957–67.

[39] Awaja F, Gilbert M, Kellya G, Foxa B, Pigram P. *Adhesion of polymers*, **Prog Polym Sci**, 2009, 34:948–68.

[40] Fourche G. *An overview of the basic aspects of polymer adhesion. Part II: Application to surface treatments*, **Polym Eng Sci**, 1995, 35(12): 968–75.

[41] Harper CA. *Background and theory. In: Harper CA, editor*, **Handbook of plastics and elastomers**, New York: McGraw-Hill, 1975.

[42] Butler CA, McCullough RL, Pitchumani R, Gillespie Jr JW. *An analysis of mechanisms governing fusion bonding of thermoplastic composites*, **J Thermoplast Compos Mater**, 1998, 11:338–63.

[43] Wool RP. *Strength of symmetric amorphous interfaces. In: Wool RP, editor*, **Polymer interfaces:**

structure and strength, Hanser/Gardner Publications Inc., 1995.

[44] Petrie EM. *Adhesives families. In: Petrie EM, editor,* **Handbook of adhesives and sealants**, McGraw-Hill, 2000.

[45] Petrie EM. *Adhesives for the assembly of aircraft structures and components. Decades of performance improvement, with the new applications of the horizon*, **Met Finish**, 2008, 106(2): 26–31.

[46] B. Lestriez, J-F Gérard, J-P Chapel, C. Plummer : *Maîtrise de la morphologie et de l'adhésion aux interfaces macroscopiques thermodurcissable/thermoplastique,* **Matériaux** (2002).

[47] Hong Ma, M. Ali Aravand, Brian G. Falzon. *Phase morphology and mechanical properties of polyetherimide modified epoxy resins: A comparative study*, **Polymer**, 179, 2019, 121640.

[48] H. S. Min, S-C Kim. *Fracture toughness of polysulfone/epoxy semi-IPN with morphology spectrum.* **Polymer Bulletin**, 42 (1999) 221-227.

[49] Y-S Kim, S-C Kim. *Properties of Polyetherimide/Dicyanate Semi-interpenetrating Polymer Network Having the Morphology Spectrum*, **Macromolecules**, 32 (1999) 2334-2341.

[50] Kinloch AJ, Shaw SJ. *The fracture resistance of a toughened epoxy adhesive*, **J Adhes**, 1981, 12:5912:5

[51] Pardoen, T., Ferracin, T., Landis, C.M., Delannay, F., *Constraint effects in adhesive joint fracture*, **J. Mech. Phys. Solids**, 2005, 53, 1951–1983.

[52] Ph. Martiny, F. Lani, A.J. Kinloch, T. Pardoen. *A maximum stress at a distance criterion for the prediction of crack propagation in adhesively-bonded joints*, **Engineering Fracture Mechanics**, 97 (2013) 105–135.

[53] K. Mimura, H. Ito, H. Fujioka. *Improvement of thermal and mechanical properties by control of morphologies in PES-modified epoxy resins***, Polymer**, 41 (2000) 4451-4459.

[54] E. Girard-Reydet, V. Vicard, J-P Pascault, H. Sautereau. *Polyetherimide-Modified Epoxy Networks: Influence of Cure Conditions on Morphology and Mechanical Properties***, Journal of Applied Polymer Science**, 65 (1997) 2433-2445.

[55] Q. Voleppe, T. Pardoen, C. Bailly. *Interdiffusion and phase separation upon curing in thermoset thermoplastic interphases unravelled by the characterization of partially cured systems*, **Polymer**, 106 (2016) 120-127.

[56] ASTM Standard D695: *Standard Test Method for Compressive Properties of Rigid Plastics.* Annual Book of ASTM Standards (2002).

[57] A.B. Ferneda, R.R. Cavacante da Costa, V. Tita, S.P. Baroncini Proenca, J. de Carvamho, B. de Moraes Purquerio. *Compression tests of castor oil biopolymer*, **Materials Research**, 9 (2006) 327-334.

[58] W.C. Oliver, G.M. Pharr, *An improved technique for determining hardness and elastic modulus using load and displacement sensing indentation experiments*, **Journal of Materials Research**, 7 (1992) 1564-1583.

[59] ASTM Standard D 5045-99: *Standard Test Method for Plane-Strain Fracture Toughness and Strain Energy Release Rate of Plastic Materials.* Annual Book of ASTM Standards (1999).

[60] Quentin Voleppe, *Characterization and modelling of the microstructure and fracture of thermoset/thermoplastic interphases*, PhD dissertation, UCLouvain, 2016.

[61] H. Tanaka, T. Araki, *Viscoelastic phase separation in soft matter: Numerical-simulation study on its physical mechanism*,**Chemical Engineering Science**, 61 (2006) 2108–2141

[62] Jérémy Chevalier, *Micromechanics of an epoxy matrix for fiber reinforced composites: experiments and physics-based modelling*, PhD dissertation, UCLouvain, 2019.

[63] A. Clausner, F. Richter. *Determination of yield stress from nanoindentation experiments*, **European Journal of Mechanics A/Solids**, 51 (2015) 11-20.

[64] M. Rodriguez, J.M. Molina-Aldarequia, C. Gonzalez, J. Llorca. *Determination of the mechanical properties of amorphous materials through instrumented nanoindentation*, **Acta Materialia**, 60, 9, 2012, 3953-3964.

[65] T. Koch, S. Seidler: *Correlations Between Indentation Hardness and Yield Stress in Thermoplastic*, ***Polymers*** **Strain**, 45 (2008) 26-33.

[66] J. Chevalier, L. Brassart, F. Lani, C. Bailly, T. Pardoen, X.P. Morelle, *Unveiling the heterogeneity-controlled viscoplastic behavior of glassy polymers*, **Journal of the Mechanics and Physics of Solids** 121 (2018) 432-446

[67] S. Dépinoy, F. Strepenne, T.J. Massart, S. Godet, T. Pardoen, *Interface toughening in multilayer materials through dissipative interlayers*, **Journal of the Mechanics and Physics of Solids,** 130 (2019) 1-20.